High-field transport and optical phonon scattering in graphene

Peter Lichtenberger,[*] Omar Morandi,[†] and Ferdinand Schürrer[‡]

Institute of Theoretical and Computational Physics, Graz University of Technology, Petersgasse 16, 8010 Graz, Austria

(Received 12 February 2010; revised manuscript received 3 March 2011; published 5 July 2011)

The coupled dynamics of electrons and optical phonons in graphene is investigated. For this purpose, a kinetic model based on space-dependent Boltzmann transport equations for electrons and optical phonons is established. This system is solved by deterministic methods that provide efficiently accurate results by dynamically treating nonequilibrium phenomena. The numerical simulations clearly show the importance of this approach when calculating *I–V* characteristics over a reasonable voltage range. Optical phonon occupations surpassing equilibrium values by factors of thousands were found which affect the charge carrier transport considerably in graphene.

DOI: 10.1103/PhysRevB.84.045406 PACS number(s): 73.50.Fq, 72.10.Di, 73.61.Wp

I. INTRODUCTION

In 2004, the preparation and characterization of the first free graphene samples[1] started a broad research on this carbon-based material. Right from the start, the high values measured for the charge carrier mobilities made graphene a very interesting candidate for applications in future nanoelectronic devices. The measured values for mobility in graphene have steadily increased in the years since 2004 and can be expected to continue to do so. Values higher than 2×10^5 cm^2/V s have been reported at room temperature.[2,3] These values significantly exceed those of conventional semiconductors and other low-dimensional systems. This amazing progress is owed to improved preparation processes, including systems of suspended graphene.[4] The electric properties of early samples were mainly determined by charged impurities within the substrate and adsorbates on the sample. The graphene sheets themselves show remarkable few defects. Now it is possible to reduce external effects on the electronic transport through graphene to a level where phonons make an important, though inevitable, contribution to the resistivity at room temperature.[5–7] When systematically eliminating all other sources of charge carrier scattering, electron-phonon scattering processes seem to determine the maximum achievable room temperature mobility. An accurate understanding of the fundamental transport processes in such high quality graphene is essential for possible future applications of graphene in electronic devices. This motivates to create a comprehensive transport model for a deeper research on the charge carrier transport in graphene.

The phonon system of graphene has already been thoroughly investigated by means of density functional theory (DFT) and Raman spectroscopy.[8–11] The obtained phonon dispersion relations and electron-phonon coupling (EPC) matrix elements are essential ingredients for kinetic models of carrier transport in single-wall carbon nanotubes (SWCNTs) and graphene. The difference between calculated EPC strengths and those deduced from transport measurements has been the major indication of an important role of self-heating in SWCNTs.[9,12] Further research[13,14] revealed that this effect is directly linked to nonequilibrium optical phonon distributions and, therefore, the electron and phonon transport in SWCNTs has to be treated on a kinetic level. These findings naturally raise the question if hot phonons are equally important for the charge carrier transport in graphene, and what a corresponding kinetic model will look like.

In this work, we will demonstrate the effects of hot phonons on the charge carrier transport in graphene in the scope of a kinetic model for electrons and phonons. We restrict ourselves to the intrinsic graphene phonon modes. We do not account for surface phonons as their influence is dependent on the substrate used and can be eliminated by suspending the graphene samples. Our model is based on semiclassical Boltzmann transport equations (BTEs) describing the time evolution of the distribution functions for electrons and optical phonons.[15] With this approach, all effects of nonequilibrium occupation numbers of electron and optical phonon states can be treated dynamically.[13,16] Therefore, we are not restricted by given assumptions on the distribution functions. In addition to the simulations presented in this paper, the kinetic model, together with the numerical scheme, forms a general framework for the kinetic transport in graphene that can be easily adopted for additional interaction processes, such as surface phonons, and more complex device geometries.

The paper is organized as follows: in Sec. II, we introduce the BTEs of electrons and optical phonons which govern the time evolution of the associated distribution functions. The necessary numerical methods, which allow us to solve the BTEs deterministically, are introduced in Sec. III. In Sec. IV, the results of simulating the charge carrier transport in doped and intrinsic graphene performed with the developed scheme are discussed. We draw concluding remarks on our work in Sec. V.

II. KINETIC MODEL

To study the charge carrier transport in graphene, we introduce a semiclassical kinetic model describing the coupled dynamics of electrons and phonons. This model is based on a set of coupled semiclassical BTEs which governs the time evolution of the distribution functions for electrons and optical phonons.[15] With this approach, effects of nonequilibrium occupation numbers of electron and optical phonon states can be treated dynamically.[13,16] This has been demonstrated for several problems in the field of carrier transport[17] including metallic CNTs.[13]

We adhere to the linear bandstructure approximation of graphene

$$\varepsilon_i(\boldsymbol{k}) = \pm\hbar v_F|\boldsymbol{k}|, \tag{1}$$

with the Fermi velocity $v_F \approx 10^6$ m/s, and treat the **K** and **K**′ valleys as one effective valley. The index i refers to the π^* band ($i = 1$, $\varepsilon_1 > 0$), and the π band ($i = 2$, $\varepsilon_2 < 0$), respectively. In the framework of the kinetic theory, the electron system is described by the electron distribution functions $f_i = f_i(\boldsymbol{x},\boldsymbol{k},t)$ which obey the Boltzmann equation[18]

$$\partial_t f_i + \boldsymbol{v}_i\,\partial_{\boldsymbol{x}} f_i - \frac{e_0}{\hbar}\boldsymbol{E}\,\partial_{\boldsymbol{k}} f_i = \mathcal{C}_i \tag{2}$$

with the group velocity $\boldsymbol{v}_i(\boldsymbol{k}) = \partial_{\boldsymbol{k}}\varepsilon_i/\hbar = \pm v_F\boldsymbol{k}/|\boldsymbol{k}|$, the electric field strength $\boldsymbol{E}$ and the elementary charge e_0; $\boldsymbol{x}$ denotes the position vector and $\boldsymbol{k}$ stands for the electron wave vector. The collision operator

$$\mathcal{C}_i = \sum_{\eta,j}\mathcal{C}_{ij}^{\eta} + \mathcal{C}_i^{EL} \tag{3}$$

accounts for scattering of electrons with different optical phonon modes η in $\mathcal{C}_{ij}^{\eta}$ including both intraband ($i = j$) and interband ($i \neq j$) processes, as well as elastic scattering processes with acoustic phonons in $\mathcal{C}_i^{EL}$. Results of DFT calculations[19] show that only three optical phonon modes contribute significantly to inelastic scattering of electrons in graphene. The first two relevant modes are longitudinal optical (LO) and transversal optical (TO) phonons with wave vectors close to the Γ point and energies of $\hbar\omega_1 = \hbar\omega_2 = 196$ meV. Because of their short wave vectors, these phonons scatter electrons within one valley. In addition, it is important to take into account zone boundary phonons with $\hbar\omega_3 = 161$ meV close to the **K** point, which are responsible for intervalley processes. We will refer to these three modes as Γ-LO, Γ-TO, and **K** phonons, and label them with the numerical indices $\eta = 1$, 2, and 3. The electron collision operator $\mathcal{C}_{ij}^{\eta}$ for the interaction of electrons with optical phonons reads

$$\mathcal{C}_{ij}^{\eta}(\boldsymbol{k}) = \frac{1}{(2\pi)^2}\int_{\mathcal{B}} d\boldsymbol{k}'\left[W_{\boldsymbol{k}'j\boldsymbol{k}i}^{\eta} f_j'(1-f_i) - W_{\boldsymbol{k}i\boldsymbol{k}'j}^{\eta}(1-f_j')f_i\right] \tag{4}$$

with $f_i = f_i(\boldsymbol{x},\boldsymbol{k},t)$ and $f_j' = f_j(\boldsymbol{x},\boldsymbol{k}',t)$. The scattering probabilities

$$W_{\boldsymbol{k}i\boldsymbol{k}'j}^{\eta} = W_{\boldsymbol{k}i\boldsymbol{k}'j}^{EM,\eta} + W_{\boldsymbol{k}i\boldsymbol{k}'j}^{AB,\eta} \tag{5}$$

accounting for phonon emission and absorption are given by

$$W_{\boldsymbol{k}i\boldsymbol{k}'j}^{EM,\eta} = s_{\boldsymbol{k}'j\boldsymbol{k}i}^{\eta}\,(1+g_{\eta}^{-})\,\delta(\varepsilon_i - \varepsilon_j' - \hbar\omega_{\eta}) \tag{6}$$

$$W_{\boldsymbol{k}i\boldsymbol{k}'j}^{AB,\eta} = s_{\boldsymbol{k}i\boldsymbol{k}'j}^{\eta}\,g_{\eta}^{+}\,\delta(\varepsilon_i - \varepsilon_j' + \hbar\omega_{\eta}) \tag{7}$$

with the energies $\varepsilon_i = \varepsilon_i(\boldsymbol{k})$ and $\varepsilon_j' = \varepsilon_j(\boldsymbol{k}')$. The delta functions $\delta(\varepsilon_i - \varepsilon_j' \pm \hbar\omega_{\eta})$ in Eqs. (6) and (7) stem from Fermi's golden rule, and ensure the conservation of energy. The scattering elements in Eqs. (6) and (7) are given by $s_{\boldsymbol{k}i\boldsymbol{k}'j}^{\eta} = \pi|D_{\boldsymbol{k}i\boldsymbol{k}'j}^{\eta}|^2/\rho\omega_{\eta}$, where $D_{\boldsymbol{k}i\boldsymbol{k}'j}^{\eta}$ are the EPC matrix elements as defined in Refs. 8, 9 and 19, and $\rho \approx 7.6\times10^{-25} kg/nm^2$ is the area density of graphene. The phonon distribution functions $g_{\eta}^{\pm} = g_{\eta}(\boldsymbol{x},\boldsymbol{q}^{\pm},t)$ are evaluated at $\boldsymbol{q}^{\pm} = \pm(\boldsymbol{k}' - \boldsymbol{k})$, ensuring the conservation of quasimomentum. It is important to note that for interband ($i \neq j$) processes $|\boldsymbol{q}^{\pm}| \leqslant \omega_{\eta}/v_F$ and for intraband ($i = j$) processes $|\boldsymbol{q}^{\pm}| \geqslant \omega_{\eta}/v_F$. This separates the optical phonons of each mode ($\eta = 1,2,3$) into two separated groups or subtypes, which we will call inter- and intraband phonons. The EPCs for Γ-LO, Γ-TO, and **K** phonons are given by

$$\left|D_{\boldsymbol{k}i\boldsymbol{k}'j}^{\mathrm{LO/TO}}\right|^2 = D_{\Gamma}^2[1 \pm \cos(\theta+\theta')], \tag{8}$$

$$\left|D_{\boldsymbol{k}i\boldsymbol{k}'j}^{\boldsymbol{K}}\right|^2 = D_{\boldsymbol{K}}^2(1 \pm \cos\theta''), \tag{9}$$

where θ denotes the angle between $\boldsymbol{k}$ and $\boldsymbol{k}' - \boldsymbol{k}$, θ' between $\boldsymbol{k}'$ and $\boldsymbol{k}' - \boldsymbol{k}$ as well as θ'' between $\boldsymbol{k}$ and $\boldsymbol{k}'$.[8,19] In the case of LO and **K** phonons, the plus sign in Eqs. (8) and (9) refers to interband processes and for TO phonons to intraband processes. The EPC coefficients are obtained from DFT calculation,[9] and their values are $D_{\Gamma}^2 = 4.560\times10^3(\mathrm{eV/nm})^2$ and $D_{\boldsymbol{K}}^2 = 9.205\times10^3(\mathrm{eV/nm})^2$. Interactions with acoustic phonons are treated in a quasielastic way by the operator

$$\mathcal{C}_i^{EL}(\boldsymbol{k}) = \frac{1}{(2\pi)^2}\int_{\mathcal{B}} d\boldsymbol{k}'\,s_{\boldsymbol{k}\boldsymbol{k}'}^{ac}\,\delta(\varepsilon_i - \varepsilon_i')(f_i - f_i'), \tag{10}$$

where $s_{\boldsymbol{k}\boldsymbol{k}'}^{ac} = \pi D_{ac}^2 k_B T(1+\cos\theta'')/\rho\hbar c_{ac}$, $D_{ac} = 16$ eV denotes the acoustic deformation potential coupling constant,[20] $c_{ac} = 2\times10^4$ ms^{-1} is the speed of sound in graphene, and k_B is the Boltzmann constant.

Similar to the electron system, the BTE for the phonon distribution $g_{\eta}(\boldsymbol{x},\boldsymbol{q},t)$ takes the form

$$\partial_t g_{\eta} + \boldsymbol{c}_{\eta}(\boldsymbol{q})\partial_{\boldsymbol{x}} g_{\eta} = \mathcal{C}_{\eta}^{OP} \tag{11}$$

with the phonon drift velocity $\boldsymbol{c}_{\eta}(\boldsymbol{q}) = \partial_{\boldsymbol{q}}\omega_{\eta}$. Here we adhere to the constant energy approximation of optical phonons and thus neglect the motion of optical phonons. The collision operator

$$\mathcal{C}_{\eta}^{OP} = \sum_{i,j}\mathcal{C}_{\eta}^{ij} + \mathcal{C}_{\eta}^{pp} \tag{12}$$

on the right-hand side of Eq. (11) consists of two parts. The operator

$$\mathcal{C}_{\eta}^{ij}(\boldsymbol{q}) = \frac{4}{(2\pi)^2}\int_{\mathcal{B}} d\boldsymbol{k}\left[W_{\boldsymbol{k}i\boldsymbol{k}^{-}j}^{EM,\eta} f_i(1-f_j^{-}) - W_{\boldsymbol{k}i\boldsymbol{k}^{-}j}^{AB,\eta}(1-f_i)f_j^{-}\right], \tag{13}$$

models the interaction with electrons [here $\boldsymbol{k}^{-} = \boldsymbol{k} - \boldsymbol{q}$ and $f_j^{-} = f_j(\boldsymbol{k}^{-},\boldsymbol{x},t)$] and

$$\mathcal{C}_{\eta}^{pp}(\boldsymbol{q}) = -\frac{1}{\tau_{\eta}}\left[g_{\eta}(\boldsymbol{q},\boldsymbol{x},t) - g_{\eta}^{0}\right] \tag{14}$$

accounts for the decay and thermalization of optical phonons according to a relaxation time approach with the optical phonon equilibrium distribution function $g_{\eta}^{0} = [\exp(\hbar\omega_{\eta}/k_B T) - 1]^{-1}$ at a constant lattice temperature T.[21] We take $\tau_{\eta} = 3.5$ ps for all phonon modes, consistent with our treatment of SWCNTs (Ref. 13) and theoretical values.[21] The factor of 4 in Eq. (13) accounts for spin and valley degeneracy.

III. NUMERICAL APPROACH

The streaming operator and the collision operators of the BTEs (2) and (11) must be discretized in such a way that the conservative properties of the equations do not get lost. Computational accuracy and efficiency are also important requirements to the numerical solution scheme. Our procedure is based on a complete discretization of the phase space of charge carriers and optical phonons. We restrict ourselves to a spatially one-dimensional problem by assuming an infinitely broad graphene sample. This implies a translational symmetry perpendicular to the electric field which defines the direction of transport. For the $\boldsymbol{k}$ space of electrons, we introduce a coordinate system based on the energy ε of the electrons and an angular variable φ measured relative to the direction of the electric field. The electron wave vector reads

$$\boldsymbol{k}(\varepsilon,\varphi) = \frac{\varepsilon}{\hbar v_F}(\cos\varphi, \sin\varphi) \tag{15}$$

in this new coordinates. We do not explicitly use band indices, as the π and the π^* bands can be unambiguously distinguished by the sign of the electron energy. Note that for negative energies ε, the definition of the polar angle deviates from the usual polar coordinates by an angle of π. This, for example, has the advantage that the angle φ directly gives the direction of the group velocity

$$\boldsymbol{v}_i(\varepsilon,\varphi) = v_F(\cos\varphi, \sin\varphi). \tag{16}$$

The momentum coordinates of optical phonons are transformed into ordinary polar coordinates (q,φ) with the modulus q of the optical phonon wave vector $\boldsymbol{q}$ and the angle φ again measured relative to the direction of the electric field which is fixed in our setup.

The spatial extension of graphene in the direction of the electric field is split up uniformly into subintervalls centered at $x_n = (n-1/2)\Delta_x$ for $n = 1,\ldots,N_x$ with $\Delta_x = L/N_x$. The length L of the device is the distance between the left and the right contacts. The energy grid is defined by $\varepsilon_n = (n - N_\varepsilon - 1/2)\Delta_\varepsilon$ for $n = 1,\ldots,2N_\varepsilon$ with a discretization step size Δ_ε. The phonon energies $\hbar\omega_\eta$ are approximated by integer multiplies of Δ_ε, i.e., $\hbar\omega_\eta \approx \hbar\tilde{\omega}_\eta = t_\eta\Delta_\varepsilon$. This facilitates the numerical evaluation of the collision integral (4), as the arguments of the delta functions in Eqs. (6) and (7) fit directly to the energy grid. The angular variable φ is discretized by $\varphi_n = 2(n-1/2)\Delta_\varphi$ for $\Delta_\varphi = 2\pi/N_\varphi$ and $n = 1,\ldots,N_\varphi$. We use the same angular discretization for the wave vectors of the electrons and optical phonons, which is not absolutely necessary, but greatly simplifies the implementation. Following this scheme, the modulus of optical phonon wave vectors q is discretized by $q_n^\eta = (n-1/2)\Delta_q^\eta$ for $n = 1,\ldots,N_q^\eta$. The choice of the parameters Δ_q^η and N_q^η must ensure that all occurring wave vectors can be handled with sufficient resolution. This is guaranteed if the conditions $\Delta_q^\eta \leqslant 2\Delta_\varepsilon/\hbar v_f$ and $N_q^\eta\Delta_q \geqslant 2N_\varepsilon\Delta_\varepsilon/\hbar v_f$ are met.

In this discretized coordinate system, the electron-phonon collision operator (4) takes the form

$$\begin{aligned}\mathcal{C}_{klm}^{ij,\eta} = \sum_{n=1}^{N_\varphi}\Big\{ & B_{lmn}^{ij,\eta-}\Big[g_{klmn}^{\eta-} f_{kl-t_\eta n}^{j}\big(1-f_{klm}^{i}\big) \\ & -\big(1+g_{klmn}^{\eta-}\big)\big(1-f_{kl-t_\eta n}^{j}\big)f_{klm}^{i}\Big]\Big\} \\ + \sum_{l=1}^{N_\varphi}\Big\{ & B_{lmn}^{ij,\eta+}\Big[\big(1+g_{klmn}^{\eta+}\big)f_{kl+t_\eta n}^{j}\big(1-f_{klm}^{i}\big) \\ & -g_{klmn}^{\eta+}\big(1-f_{kl+t_\eta n}^{j}\big)f_{klm}^{i}\Big]\Big\}\end{aligned} \tag{17}$$

with the discretized electron distribution functions $f_{klm}^i = f_i(x_k,\boldsymbol{k}(\varepsilon_l,\varphi_m),t)$ and $f_{kl\pm t_\eta n}^j = f_i(x_k,\boldsymbol{k}(\varepsilon_l \pm \hbar\tilde{\omega}_\eta,\varphi_n),t)$ and the scattering element

$$B_{lmn}^{ij,\eta\pm} = \frac{1}{(2\pi\hbar v_F)^2}\big|\varepsilon_{l\pm t_\eta}\big|\Delta_\varphi s_{ij}^\eta\big(\varepsilon_l,\varphi_m,\varepsilon_{l\pm t_\eta},\varphi_n\big). \tag{18}$$

It is easy to see that the electron distribution functions need to be evaluated only at grid points, as the energy discretization is adjusted to the optical phonon energies $\hbar\omega_\eta$.[13] This cannot be assured for phonon distribution functions $g_\eta(\boldsymbol{q})$. In the discrete collision term (17), $g_{klmn}^{\eta\pm} = g_\eta(x_k,\boldsymbol{q}_{klmn}^{\eta\pm})$ has to be evaluated at

$$\boldsymbol{q}_{klmn}^{\eta\pm} = \pm\big[\boldsymbol{k}(\varepsilon_l,\varphi_m) - \boldsymbol{k}\big(\varepsilon_{l\pm t_\eta},\varphi_n\big)\big] \tag{19}$$

which in general is not a grid point for optical phonons. This necessitates an interpolation to obtain a value for $g_{klmn}^{\eta\pm}$ in terms of the values of the surrounding grid points. We use a linear interpolation with suitable coefficients to ensure the conservation of energy and momentum.

The derivatives $\partial_{\boldsymbol{x}}$ and $\partial_{\boldsymbol{k}}$ on the left hand side of Eq. (2) transform into derivatives with respect to the spatial variable x, the energy ε, and the angle φ. All derivatives are approximated numerically with a fifth-order weighted essentially nonoscillatory (WENO) finite-difference scheme.[22] The application of the discretization scheme and the approximation of derivatives leads to a system of $(2N_\varepsilon + 3N_q)N_\varphi N_x$ coupled ordinary differential equations. The time-dependent derivatives of Eqs. (2)–(11) are approximated by a Runge-Kutta method of third order with total variation diminishing (TVD) properties.[23]

IV. SIMULATION RESULTS

In our simulations, we use the following grid parameters: $N_\varepsilon = 80$ with $\Delta_\varepsilon = 20meV$, $N_\varphi = 8$, and $N_x = 12$. The parameters for phonon wave vectors are automatically determined by $N_q \geqslant N_\varepsilon$ and $\Delta_q \leqslant 2\Delta_\varepsilon/\hbar v_f$. This ensures that all occurring wave vectors are covered with sufficient resolution.

As a first step, we consider the ballistic charge carrier transport in graphene. The results are shown in the left plot of Fig. 1. The most striking feature is a current saturation, whose value depends on the Fermi level and, therefore, on the carrier concentration. This is completely different to the case of metallic SWCNTs, where the current does not saturate, but shows a linear increase of the current with the applied voltage U:[13] $J = 4e_0^2U/h$. In the case of graphene, saturation is found at $J_{\text{sat}} = e_0 v_F N_0/\pi$, with the equilibrium carrier density N_0, for $e_0U > \varepsilon_F$. This limit can be deduced from the boundary conditions. If the applied voltage is high enough so that all electrons that enter the sample at the positive contact with energies up to about ε_F can invert their direction within the sample, the current is determined by the electrons entering at the negative contact. The saturation current is given by all

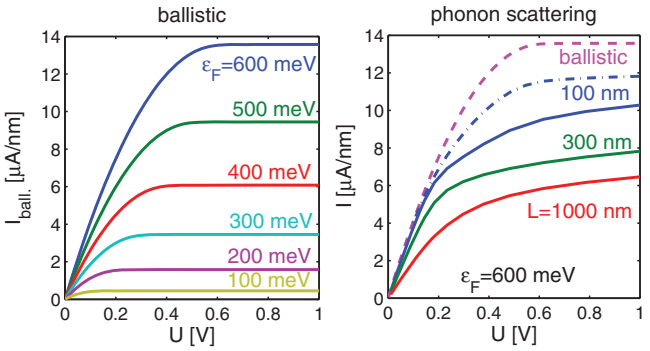

FIG. 1. (Color online) (Left panel) Current-voltage characteristics for the ballistic transport in contacted graphene for several Fermi levels. (Right panel) Current density vs voltage for different sample lengths at a Fermi energy of 600 meV with a full dynamic treatment of optical phonons (solid lines). A kink, associated to the optical phonon emission processes at $U \approx 0.2$ V can be noticed. For comparison, the length-independent case of ballistic transport (dashed line) and the simplified case of a constant phonon distribution at $T = 300$ K for the shortest ($L = 100$ nm) sample (dash-dotted line) are included.

inflowing electrons due to the equilibrium distribution given at the boundary weighted by the projection of their velocity vectors onto the direction of the electric field (x axis).

This is a completely different behavior with respect to that of metallic SWCNTs because of two reasons. First, in SWCNTs, there is no way to change the flight direction of electrons in the ballistic case, as they stay either left or right moving electrons traveling with the Fermi velocity.[24] This is not true for graphene, as the electric field can change the direction of the momentum vector and, therefore, the direction of the motion of the electrons. Second, closely related to the first reason, in graphene, the π and π^* electrons are separated in the semiclassical picture. The electric field cannot move electrons over the Dirac point, as in SWCNTs. Hence, the number of free carriers within each band is preserved. These differences between graphene and SWCNTs originate from the different dimensionality of the two systems.

In a next step, we study the influence of optical phonons in a system with $\varepsilon_F = 600$ meV ($N_0 = 2.7 \times 10^{13}$ cm^{-2}) to clearly separate optical phonon effects from ballistic saturation phenomena. The calculated I–V characteristics for graphene samples of different lengths are depicted as solid lines in the right panel of Fig. 1. A noticeable kink in the characteristics can be seen at $U \approx 0.2$ V. This can be explained by the onset of optical phonon emission processes when electrons have gained enough energy to emit optical phonons. The deviation from ballistic transport at low bias is attributed to acoustic phonons. For long samples, this effect becomes quite dominant by scattering many electrons before they reach sufficient energies to emit an optical phonon.

To estimate the importance of a full dynamical treatment of optical phonons, we compare the results with those obtained by keeping the phonons in equilibrium at room temperature ($T = 300$ K). The corresponding I–V characteristic for a graphene sample with a length of 100 nm is shown as a dash-dotted line in the right panel of Fig. 1. It can be clearly seen that the simplified kinetic model significantly underestimates the influence of optical phonons on the I–V characteristic.

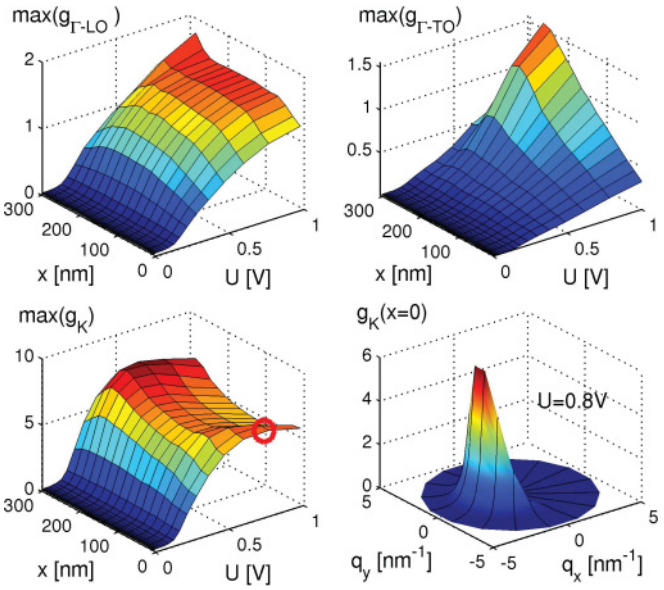

FIG. 2. (Color online) Maximum of the distribution functions of Γ-LO, Γ-TO, and **K** phonons at steady state vs the applied voltage and the position along the transport direction in the sample. The Fermi level is 600 meV. Additionally, the distribution function of the **K** phonons for a voltage of $U = 0.8$ V at the drain contact $x = 0$ nm (corresponding to the circle in the bottom left panel) is given in the bottom right panel.

A look at the optical phonon distribution functions allows us to examine this result more closely. In Fig. 2, the maximum occupation numbers, $\max_{\boldsymbol{q}} g_\eta(x,q,\varphi)$, along the graphene sample are plotted as a function of the voltage. It is evident that the distribution functions dramatically exceed the equilibrium values of $g_\Gamma \approx 4.4 \times 10^{-4}$ and $g_{\mathbf{K}} \approx 2.1 \times 10^{-3}$ at $T = 300$ K and the assumption $g \ll g + 1$ no longer holds, which makes absorption processes equally important. Of course, the maximum value is not necessarily representative for the whole distribution. However, looking at the phonon distribution function depicted in the bottom right panel of Fig. 2, reveals that a significant number of phonon states become highly excited highlighting the nonequilibrium character and the need for a dynamical treatment. The comparison of the plots for the different phonon modes shows that the **K** phonons reach the highest excitation. This can be attributed to their higher EPC matrix element and to the lower energy of these phonons. Nevertheless, we find occupation numbers $g_\eta \gg 1$ for all optical phonon modes. Bulk calculations show much lower excitations,[5,17] even if exactly the same scattering processes are considered.[17] This highlights the importance of a space-dependent treatment of the transport equations for systems close to the ballistic regime.

In a setup with a Fermi level of $\varepsilon_F = 600$ meV, the π band does not contribute to the charge carrier transport and interband processes can be neglected. However, in the case of intrinsic graphene, these processes become effective and produce interesting effects. The results obtained for intrinsic graphene are presented in Fig. 3. We again compare the I–V characteristics for the cases of ballistic transport, hot phonons, and a fixed equilibrium phonon background. The ballistic current saturates well before optical phonon

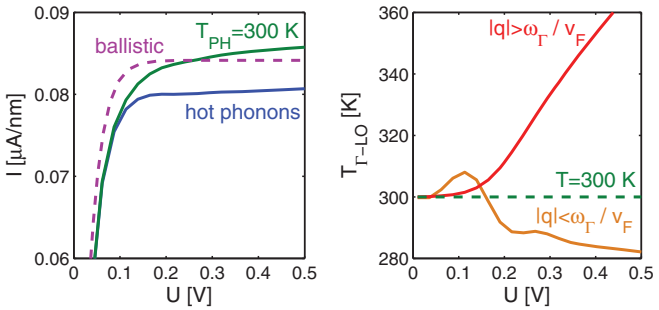

FIG. 3. (Color online) Voltage dependencies of the current and phonon temperatures in intrinsic ($\varepsilon_F = 0$ meV) graphene. (Left panel) I–V characteristic for the case of ballistic transport, hot phonons, and equilibrium phonons for $T_{\rm PH} = 300$ K. (Right panel) Temperatures of Γ-LO phonons with long and short wave vectors in dependence on the applied voltage.

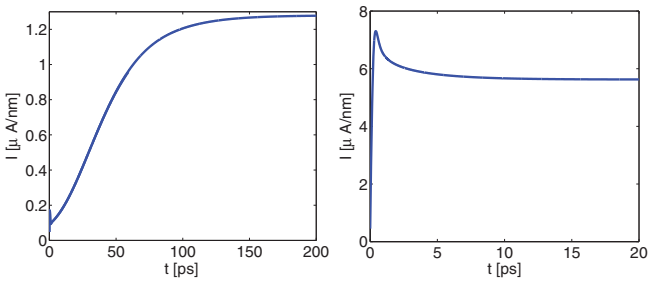

FIG. 4. (Color online) Transient current evolution: (left plot) intrinsic graphene; (right plot) $\epsilon_F = 600$ meV.

emission can occur at $U \approx 0.2$ V. In the low bias regime, ($U \lesssim 0.1$ V) the main contribution to the resistivity comes from the acoustic phonons, and no significant difference is observed between calculations performed with hot phonons and phonons in equilibrium at 300 K. In contrast, for high fields, a significant deviation between the influence of hot and equilibrium phonons arises. When fixing the optical phonons to their equilibrium, the current can even surpass the ballistic current. This unexpected behavior can be explained by the fact that interband processes, which scatter electrons into the π^* band, generate new electron-hole pairs which additionally contribute to the current. Such a process is always linked with the absorption of phonons with short wave vectors. This can be clearly seen, by looking at the right panel of Fig. 3, where the temperatures of Γ-LO phonons with long and short wave vectors, deduced from averaged occupation numbers, are plotted as a function of the applied voltage. The optical phonons responsible for the generation of electron-hole pairs become significantly cooler, which means that they deplete, and thus reduce the electron-hole pair generation rate. Keeping the phonons fixed at 300 K leads to higher electron-hole generation rates, and explains the overestimation of the current in this case. The peak at $U = 0.1$ V can be explained by the emission of phonons when both electrons and holes (vacancies below the Dirac point) have reached energies of 100 and −100 meV, respectively, which opens an emission channel. At higher voltages, this effect is superseded by generation processes through absorption.

A. Time evolution

We study the transient response of the electron-hole and phonon gas to the abrupt change of the applied bias. As initial datum, for $t = 0$, we assume that the graphene sheet is in the stationary state for an applied voltage U equal to 0.01 V. For $t > 0$, we impose $U = 0.1$ V. In Fig. 4, we show the evolution of the total current at the drain contact for the intrinsic ($\varepsilon_F = 0$) and doped graphene ($\varepsilon_F = 600$ meV). The simulations put in evidence the remarkable difference in the time scale of the evolution for the current in intrinsic and nonintrinsic graphene. In particular, a comparison with analogous results for SWCNTs, reveals that the time scale of the evolution of the current in graphene agrees with SWCNTs only for the high-doped case, whereas in the intrinsic case, the evolution is significantly slower.[25] As explained below, the reason for this difference is connected with the need of a large number of optical phonons to perform interband transitions in intrinsic graphene. This is in contrast to the phonon-free excitations of electron-hole pairs in SWCNTs. A careful analysis of the Boltzmann collision operator reveals that the reason for this time scale difference can be attributed to the specific kind of phonon scattering processes which are responsible for the dynamics of the particle gas. In particular, for non-intrinsic graphene, the relatively fast response of the system to the external stimulus is caused by the activation of a strong phonon emission process. In this regime, the system is able to dissipate efficiently the kinetic energy imparted to the particles by the external field. On the contrary, when dealing with intrinsic graphene, the main mechanism that modifies the current by driving the initial low-biased configuration to the final high-field state, is the interband transfer of particles caused by absorbtion of optical phonons. Since the latter is an emission process, it is proportional to the occupation number of phonons $g_\eta(\mathbf{q}) \propto 10^{-2}$ (with $|\mathbf{q}| < \omega_\Lambda / v_F$). This justifies the difference in the time scale of the current evolution between intrinsic (mainly adsorption interband processes proportional to g_η) and nonintrinsic graphene (emission processes proportional to $1 + g_\eta$). In order to make this point more clear, in Fig. 5, we depict the evolution of the phonon distribution function $g_{\mathbf{K}}$. The plot reveals both the temporal increase of the phonon occupation numbers induced by thermal dispersion and its deep depletion around $\mathbf{q} = 0$. The latter marks the strong phonon adsorption regime which characterizes the strongly out-of-equilibrium state in the presence of a high potential in intrinsic graphene.

B. Lattice heating

The phonon modes are the only dissipative channels through which the electrons can loose the energy imparted by the external field. High currents may induce a significant overpopulation of phonons. A considerable heating of the silicon oxide in FETs with a graphene channel under a high applied source-drain voltage has been observed. This indicates the non-negligible Joule effect induced by the strong current flux.[26] Under these conditions, the acoustic phonon distribution cannot be assumed to remain at a fixed temperature T_L. Furthermore, experiments have shown that the temperature under the silicon oxide in the silicon substrate is mainly unaffected by the Joule heating, but this is not true for the graphene sheet itself.

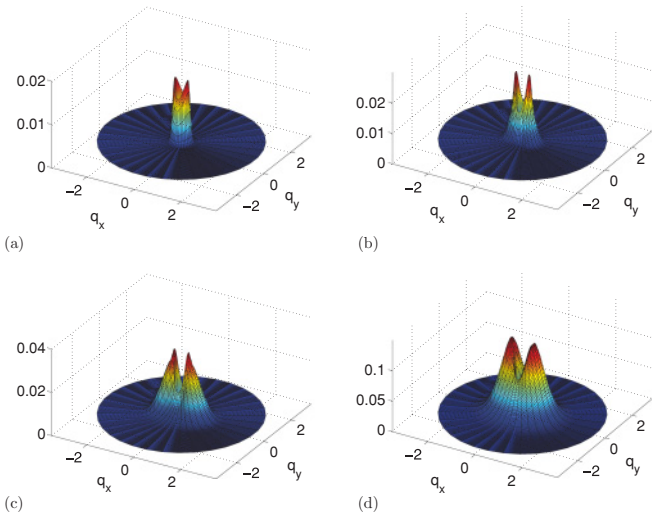

FIG. 5. (Color online) Phonon distribution $g_{\mathbf{K}}$ for (a) $t = 0$, (b) $t = 0.3$ ps, (c) $t = 1$ ps, and (d) $t = 10$ ps.

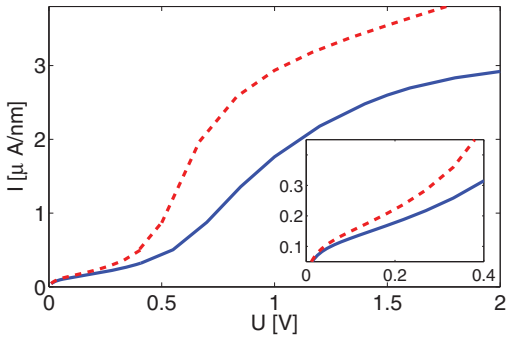

FIG. 6. (Color online) Total current in graphene when the lattice heating is included phenomenologically by Eq. (20). Continuous blue line: nonequilibrium phonon solution and dashed red line: optical phonons at the equilibrium.

Experimental evidence has recently confirmed that optical phonons are significantly heated in high-field regimes which results in a high nonequilibrium state of optical phonons.[27] In particular, direct measurements of the temperature, preformed by spatially resolved Raman spectroscopy, showed that at the interior of biased graphene sheets, hot spots appear, where the phonon temperature can raise above 1600 K. This confirms the presence of a large non-equilibrium population of phonons.[26]

For these reasons, in our simulations, we include the dependence of the lattice heating on the optical phonon decay process. The microscopic characterization of phonon decays includes anharmonic effects represented by multiphonon processes and virtual electron-hole excitations. Although in the simplest scenario, phonons will decay into two acoustic phonons, a comprehensive treatment of this process would require the solution of the Boltzmann equation by including the phonon-phonon collision operator. The latter becomes a formidable task for a direct numerical treatment and, since the details of the scattering are not completely understood, it would reveal itself to be a probable source of unchecked errors.[21] In our system, the flux of particles and energy between optical and acoustic phonons is modeled by a simple relaxation process, where the phonon distribution function tends toward a local Bose-Einstein distribution at the temperature T [see Eq. (14)]. In the previous simulations, the acoustic phonon temperature was considered to be equal to the constant lattice temperature T_L (consequently also the relaxation time τ_η was constant). Here, according to Ref. 28, we study the effect of lattice heating by inserting in our model the following empirical dependence of T upon the total current flowing in the graphene sheet:

$$T = T_L + \gamma \frac{IU}{L} \tag{20}$$

with $\gamma = 0.3 \times 10^3$ W cm^{-2} K^{-1}. Concerning the phonon relaxation time, we assume $\tau_\eta(T) = \tau_c + \frac{\tau_h - \tau_c}{T_h - T_c}(T - T_c)$ with $\tau_c = 5$ ps ($T_c = 300$ K) and $\tau_h = 3$ ($T_h = 800$ K). These linear formulas are in a good agreement with experiments (see Ref. 21 for the theoretical study and the experiments concerning the linear dependence of τ vs T). A look at Eq. (20) reveals that the temperature of the substrate significantly increases only for a high applied voltage, giving a contribution spanning from a few Kelvin for $U = 0.1$ V until a factor of the order of hundred Kelvin for higher values ($U \sim 1$ V). The numerical results given in Fig. 6 show that the increase of the acoustic phonon temperature entails a consequent rise of the total current. This unexpected result can be easily explained by noting that a hotter phonon distribution supports the generation of new particle-hole pairs, which rise the total number of charged particles in the channel. The comparison with the assumption of an equilibrium for the phonon distribution shows that in the latter case, the current is significantly overestimated. This justifies the need of a full dynamic treatment of the phonon occupation numbers.

Recently, simulations based on a Boltzmann transport equation, where optical phonons are considered to be in thermal equilibrium, have been published.[27,30–32] Although our simulations and experiments show that optical phonons are out-of-equilibrium, the simpler assumption of a thermal optical phonon bath can be invoked for reproducing the I–V characteristics observed. A key role in this discussion is played by the Joule self-heating of the graphene channel. In fact, as found by means of our simulations (and that is also confirmed by the calculations reported in Refs. 30 and 31), the final value of the current flow depends sensibly on Eq. (20) and the factor γ. In particular, in Ref. 31, the latter is considered as a fitting parameter exploited to let the simulations be conformed with experiments. Our more detailed treatment of the scattering process tells us that there is an *observable* difference between the particle motion in the presence of an equilibrium phonon gas compared to one characterized by a fully resolved nonequilibrium phonon distribution. As shown in Fig. 6, these non-negligible corrections are of the same order as the modification of the current induced by self-heating. For that reason, we think that using the value of γ and consequently the phonon temperature as a fitting parameter can in a certain way compensate the minor precision of the simplified model applied in Ref. 31. On the contrary, a clear indication of the nonequilibrium character of the phonon gas is given by the time scale of the carrier evolution where, as explained in Sec. IV A, the phonon density depletion around the Dirac point forces

the evolution of the system to proceed faster or slower as a function of the chemical potential.

V. CONCLUSION

The obtained results, in this study, clearly reveal the important influence of optical phonons on the charge carrier transport in high-quality graphene at temperatures and applied voltages highly relevant to future applications in electronic devices. We clearly show that at room temperature in the near-ballistic regime, nonequilibrium optical phonons together with contact effects limit the possible current. Under this condition, we find highly excited optical phonons with significant impact on the electronic properties of graphene. The effects caused by nonequilibrium optical phonons are similar to those found in SWCNTs. These results required a space-dependent simulation, as these effects are not accessible by numerical studies of bulk materials.[5,17,33] Our kinetic model describes these phenomena in an efficient and detailed manner.

ACKNOWLEDGMENTS

This work has been supported by the Austrian Science Fund, Vienna, under the Contract No. P 21326-N 16. We are very grateful to S. Piscanec and A. C. Ferrari for many useful discussions.

*lichtenb@itp.tugraz.at
†morandi@dipmat.univpm.it
‡schuerrer@itp.tugraz.at

[1] K. S. Novoselov, A. K. Geim, S. V. Morozov, D. Jiang, Y. Zhang, S. V. Dubonos, I. V. Grigorieva, and A. A. Firsov, Science **306**, 666 (2004).
[2] K. I. Bolotin, K. J. Sikes, Z. Jiang, M. Klima, G. Fudenberg, J. Hone, P. Kim, and H. L. Stormer, Solid State Commun. **146**, 351 (2008).
[3] S. V. Morozov, K. S. Novoselov, M. I. Katsnelson, F. Schedin, D. C. Elias, J. A. Jaszczak, and A. K. Geim, Phys. Rev. Lett. **100**, 016602 (2008).
[4] X. Du, I. Skachko, A. Barker, and E. Y. Andrei, Nat. Nanotech. **3**, 491 (2008).
[5] A. Barreiro, M. Lazzeri, J. Moser, F. Mauri, and A. Bachtold, Phys. Rev. Lett. **103**, 076601 (2009).
[6] V. E. Dorgan, M.-H. Bae, and E. Pop, Appl. Phys. Lett. **97**, 082112 (2010).
[7] R. Murali, Y. Yang, K. Brenner, T. Beck, and J. D. Meindl, Appl. Phys. Lett. **94**, 243114 (2009).
[8] S. Piscanec, M. Lazzeri, F. Mauri, A. C. Ferrari, and J. Robertson, Phys. Rev. Lett. **93**, 185503 (2004).
[9] M. Lazzeri, S. Piscanec, F. Mauri, A. C. Ferrari, and J. Robertson, Phys. Rev. Lett. **95**, 236802 (2005).
[10] A. C. Ferrari, J. C. Meyer, V. Scardaci, C. Casiraghi, M. Lazzeri, F. Mauri, S. Piscanec, D. Jiang, K. S. Novoselov, S. Roth *et al.*, Phys. Rev. Lett. **97**, 187401 (2006).
[11] M. Lazzeri, S. Piscanec, F. Mauri, A. C. Ferrari, and J. Robertson, Phys. Rev. B **73**, 155426 (2006).
[12] E. Pop, D. Mann, J. Cao, Q. Wang, K. Goodson, and H. Dai, Phys. Rev. Lett. **95**, 155505 (2005).
[13] C. Auer, F. Schürrer, and C. Ertler, Phys. Rev. B **74**, 165409 (2006).
[14] M. Lazzeri and F. Mauri, Phys. Rev. B **73**, 165419 (2006).
[15] B. K. Ridley, *Quantum Processes in Semiconductors* (Oxford University Press, Oxford, 1999).
[16] P. Lichtenberger, C. Auer, and F. Schürrer, Transp. Theory Stat. Phys. **36**, 299 (2007).
[17] C. Auer, P. Lichtenberger, and F. Schürrer, Eur. Phys. J. B **70**, 133 (2009).
[18] M. Lundstrom, *Fundamentals of Carrier Transport* (Cambridge University Press, Cambridge, 2000).
[19] S. Piscanec, M. Lazzeri, J. Robertson, A. C. Ferrari, and F. Mauri, Phys. Rev. B **75**, 035427 (2007).
[20] E. H. Hwang and S. DasSarma, Phys. Rev. B **77**, 115449 (2008).
[21] N. Bonini, M. Lazzeri, N. Marzari, and F. Mauri, Phys. Rev. Lett. **99**, 176802 (2007).
[22] G. Jiang and C.-W. Shu, J. Comput. Phys. **126**, 202 (1996).
[23] C.-W. Shu and S. Osher, J. Comput. Phys. **77**, 439 (1988).
[24] Z. Yao, C. L. Kane, and C. Dekker, Phys. Rev. Lett. **84**, 2941 (2000).
[25] C. Auer, F. Schüerrer, and C. Ertler, J. Comput. Electron. **6**, 325 (2007).
[26] D-H. Chae, B. Krauss, K. V. Klitzing, and J. H. Smet, Nano Lett. **10**, 466 (2010).
[27] S. Berciaud, M. Y. Han, K. F. Mak, L. E. Brus, P. Kim, and T. F. Heinz, Phys. Rev. Lett. **104**, 227401 (2010).
[28] M. Freitag, M. Steiner, Y. Martin, V. Perebeinos, Z. Chen, J. C. Tsang, and Ph. Avouris, Nano Lett. **9**, 1883 (2009).
[29] R. Bistritzer and A. H. MacDonald, Phys. Rev. B **80**, 085109 (2009).
[30] A. M. DaSilva, K. Zou, J. K. Jain, and Jun Zhu, Phys. Rev. Lett. **104**, 236601 (2010).
[31] V. Perebeinos and P. Avouris, Current saturation and surface polar phonon scattering in graphene, e-print arXiv:0910.4665v1.
[32] J.-A. Yan, W. Y. Ruan, and M. Y. Chou, Phys. Rev. B **79**, 115443 (2009).
[33] A. Akturk and N. Goldsman, J. Appl. Phys. **103**, 053702 (2008).